

200 kV). Specimens for scanning electron microscopy were fixed to a piece of copper tape and soaked in 2 M NaOH for 0.5 h to remove the alumina template. After careful rinsing with deionized water in three static rinse baths, the tape was attached to the SEM stub and sputtered with about a 5 nm layer of gold. SEM images were obtained using a Hitachi X650/EDAX, PV9100 SEM, and a JEOL 5610 LV SEM. The chemical compositions of the nanotubes and composite nanostructures were characterized by energy dispersive spectroscopy, which was performed in the scanning electron microscope with a WD-8 analyzer. The room-temperature magnetic characterization of the arrays of composite nanostructure was performed by using a Lake Shore 7303-9309 vibrating sample magnetometer (VSM).

Received: May 18, 2002  
Final version: July 19, 2002

## Antimony Trisulfide Inverted Opals: Growth, Characterization, and Photonic Properties\*\*

By Beatriz H. Juárez, Silvia Rubio, José Sánchez-Dehesa, and Cefe López\*

The control of light propagation inside materials is a major goal in materials science. In this sense, the fabrication of structures with complete photonic bandgaps (PBGs) is particularly interesting.<sup>[1,2]</sup> In these structures where the dielectric constant is spatially modulated, a certain range of light frequencies may not be allowed to exist within the crystal, regardless of the propagation direction. The applications of these structures, called photonic crystals (PCs),<sup>[3]</sup> are especially remarkable when they work in the visible (VIS) and near infrared (NIR) regions of the spectrum of light. The most important features of the PC are mainly given by the topology of the structure and the dielectric constant contrast of the materials composing the PC, defined as  $\nu = \max(\epsilon_m/\epsilon_s, \epsilon_s/\epsilon_m)$ ,  $\epsilon_m$  being the background medium dielectric constant and  $\epsilon_s$  the same parameter for the scattering centers. It is necessary, in addition, that the lattice parameter of the structure be of the order of the wavelength of light. In the last few years, two different techniques have provided the most significant successes, namely, lithography<sup>[4,5]</sup> and colloidal self-assembly.<sup>[6]</sup> A new method based on nanorobotic manipulation to build diamond-like structures is also offering outstanding results.<sup>[7]</sup> Sözüer et al.<sup>[8]</sup> demonstrated that a face-centered-cubic (fcc) arrangement of air spheres in a high dielectric constant matrix ( $\epsilon_m > 8.4$ )<sup>[9]</sup> shows a complete PBG between the eighth and the ninth photonic bands. Experimentally, it is possible to fabricate such a structure starting from a synthetic opal (made of silica or latex spheres), loading it with a convenient material and, finally, etching the spheres away. These 3D structures are known as inverse opals.<sup>[10-14]</sup> To date, only inverse opals made of silicon<sup>[13]</sup> or germanium<sup>[14]</sup> have shown evidence of a complete PBG in the NIR. However, to the best of our knowledge, no inverse opals with a PBG in the VIS have been presented. The reason for this lies in the limited number of materials transparent in the VIS range with a high enough dielectric constant.

Here, we present the first inverse opal made from a chalcogenide whose optical properties should lead to the achieve-

- [1] S. Iijima, *Nature* **1991**, 354, 56.  
 [2] a) M. Terrones, N. Grobert, W. K. Hsu, Y. Q. Zhu, W. B. Hu, H. Terrones, J. P. Hare, H. W. Kroto, D. R. M. Walton, *MRS Bull.* **1999**, 24, 43. b) M. Freemantle, *Chem. Eng. News* **1996**, 74(14), 62. c) J. Sloan, J. Cook, M. L. H. Green, J. L. Hutchison, R. Tenne, *J. Mater. Chem.* **1997**, 7, 1089.  
 [3] a) Y. Wu, P. Yang, *Adv. Mater.* **2001**, 13, 520. b) G. Che, B. B. Lakshmi, E. R. Fisher, C. R. Martin, *Nature* **1998**, 393, 346.  
 [4] a) P. M. Ajayan, S. Iijima, *Nature* **1993**, 361, 333. b) P. M. Ajayan, T. W. Ebbesen, T. Ichihashi, S. Iijima, K. Tanigaki, H. Hiura, *Nature* **1993**, 362, 522.  
 [5] a) S. C. Tsang, Y. K. Chen, P. J. F. Harris, M. L. H. Green, *Nature* **1994**, 372, 159. b) A. Chu, J. Cook, J. R. Heesom, J. L. Hutchison, M. L. H. Green, J. Sloan, *Chem. Mater.* **1996**, 8, 2751. c) R. M. Lago, S. C. Tsang, K. L. Lu, Y. K. Chen, M. L. H. Green, *J. Chem. Soc., Chem. Commun.* **1995**, 1355. d) S. C. Tsang, J. J. Davis, M. L. H. Green, H. A. O. Hill, Y. C. Leung, P. J. Sadler, *J. Chem. Soc., Chem. Commun.* **1995**, 1803. e) Y. L. Hsin, K. C. Hwang, Fu-Rong Chen, Ji-Jung Kai, *Adv. Mater.* **2001**, 13, 830. f) S. Fullam, D. Cottell, H. Rensmo, D. Fitzmaurice, *Adv. Mater.* **2000**, 12, 1430.  
 [6] a) S. Subramoney, *Adv. Mater.* **1998**, 10, 1157. b) J. Y. Dai, J. M. Lauerhaas, A. A. Setlur, R. P. H. Chang, *Chem. Phys. Lett.* **1996**, 258, 547.  
 [7] a) N. Grobert, M. Terrones, O. J. Osborne, H. Terrones, W. K. Hsu, S. Trasobares, Y. Q. Zhu, J. P. Hare, H. W. Kroto, D. R. M. Walton, *Appl. Phys.* **1998**, A67, 595. b) B. K. Pradhan, T. Kyotani, A. Tomita, *Chem. Commun.* **1999**, 1317. c) T. Kyotani, L.-F. Tsai, A. Tomita, *Chem. Commun.* **1997**, 701.  
 [8] a) W. K. Hsu, J. P. Hare, M. Terrones, P. J. F. Harris, H. W. Kroto, D. R. M. Walton, *Nature* **1995**, 377, 687. b) W. K. Hsu, H. Terrones, M. Terrones, N. Grobert, A. I. Kirkland, J. P. Hare, K. Prassides, P. D. Townsend, H. W. Kroto, D. R. M. Walton, *Chem. Phys. Lett.* **1998**, 284, 177. c) W. K. Hsu, J. Li, H. Terrones, M. Terrones, N. Grobert, Y. Q. Zhu, S. Trasobares, J. P. Hare, C. J. Pickett, H. W. Kroto, D. R. M. Walton, *Chem. Phys. Lett.* **1999**, 301, 159.  
 [9] B. K. Pradhan, T. Toba, T. Kyotani, A. Tomita, *Chem. Mater.* **1998**, 10, 2510.  
 [10] a) N. Grobert, M. Mayne, M. Terrones, J. Sloan, R. E. Dunin-Borkowski, R. Kamalakaran, T. Seeger, H. Terrones, M. Rühle, D. R. M. Walton, H. W. Kroto, J. L. Hutchison, *Chem. Commun.* **2001**, 471. b) V. M. Cepak, J. C. Hulteen, G. Che, K. B. Jirage, B. B. Lakshmi, E. R. Fisher, C. R. Martin, *J. Mater. Res.* **1998**, 13, 3070.  
 [11] a) G. Che, B. B. Lakshmi, C. R. Martin, E. R. Fisher, *Chem. Mater.* **1998**, 10, 260. b) J. Li, C. Papadopoulos, J. M. Xu, M. Moskovits, *Appl. Phys. Lett.* **1999**, 75, 367.  
 [12] T. Iwasaki, T. Motoi, T. Den, *Appl. Phys. Lett.* **1999**, 75, 2044.  
 [13] S. Chikazumi, *Physics of Magnetism*, John Wiley and Sons, New York **1964**.  
 [14] a) T. M. Whitney, J. S. Jiang, P. C. Searson, C. L. Chien, *Science* **1993**, 261, 1316. b) D. Li, L. Dai, S. Huang, A. W. H. Mau, Z. L. Wang, *Chem. Phys. Lett.* **2000**, 316, 349.

[\*] Dr. C. López, B. H. Juárez, S. Rubio  
 Instituto de Ciencia de Materiales de Madrid (CSIC)  
 Cantoblanco, E-28049 Madrid (Spain)  
 and  
 Unidad Asociada UPV-CSIC  
 Camino de Vera s/n, E-46022 Valencia (Spain)  
 E-mail: cefe@icmm.csic.es  
 J. Sánchez-Dehesa  
 Dep. Física Teórica de la Materia Condensada  
 Universidad Autónoma de Madrid  
 Cantoblanco, E-28049 Madrid (Spain)

[\*\*] This work was partially financed by the Spanish CICYT project MAT2000-1670-C04 and the European Commission Project IST-1999-19009 PHOBOS. The authors thank Prof. F. Meseguer, Dr. A. Blanco, F. García-Santamaría, and Dr. J. M. Palacios for full support.

ment of a PBG in the VIS. The selected material is antimony trisulfide,  $\text{Sb}_2\text{S}_3$ .

The mineral, with an orthorhombic crystalline<sup>[15]</sup> structure, is known as stibnite. The absorption edge of  $\text{Sb}_2\text{S}_3$  thin films lies at 2.2 eV (564 nm) for the amorphous form and at 1.78 eV (697 nm) for the crystalline state.<sup>[16]</sup> In the transparency region the value of the dielectric constant varies from 9.6 to 10.9 in the amorphous material and from 13.6 to 14.4 in the crystalline state.<sup>[17]</sup> In both cases it is high enough to obtain a PBG: in the first case, in the VIS range from 564 nm, and in the second one, in the NIR from 700 nm.

Several methods have been reported to grow  $\text{Sb}_2\text{S}_3$  thin films, such as chemical bath deposition (CBD) in non-aqueous<sup>[18]</sup> and aqueous media,<sup>[19–21]</sup> vacuum evaporation,<sup>[22,23]</sup> spray pyrolysis,<sup>[24,25]</sup> and flash evaporation,<sup>[26]</sup> as well as others to obtain precipitated powders.<sup>[27]</sup> None of the recipes based on CBD methods provides successful results in terms of the infiltration of opal matrices. Most authors use complexing agents such as oxalic or tartaric acids to control the growth of thin films and avoid the fast precipitation resulting from direct mixing of two solutions containing  $\text{Sb}^{3+}$  cations and  $\text{S}^{2-}$  anions. Following the CBD methods, thin films of  $\text{Sb}_2\text{S}_3$  grew on the opal surface and prevented further growth in the internal interstices. In addition, trying to grow the material in consecutive steps or baths dissolves the previously synthesized material. On one hand,  $\text{Sb}_2\text{S}_3$  is dissolved in a new  $\text{SbCl}_3$  aqueous medium probably due to protonation of the sulfur ion to give  $\text{H}_2\text{S}$ . On the other hand, it is a well-known fact that stibnite can be dissolved in media containing sulfide ions, resulting in hydrosoluble anionic species.<sup>[28]</sup>

Here, we demonstrate that precipitation of amorphous  $\text{Sb}_2\text{S}_3$  followed by subsequent annealing provides stable enough structures to withstand silica etching and leads to inverted structures. In this work, we have obtained infilling ratios of up to ca. 100 % of the pore volume. The process, assisted by a suction system, begins with the precipitation of amorphous antimony trisulfide. Although CBD is often performed using a single bath we used two different  $\text{Sb}^{3+}$  and  $\text{S}^{2-}$  ion-containing baths, antimony trichloride and thioacetamide aqueous solutions, respectively. No extra agents were used to complex the antimony source.

By means of the precipitation method, several opals with different sphere diameters were loaded with  $\text{Sb}_2\text{S}_3$ . Various techniques were applied to characterize the samples: Raman spectroscopy, scanning electron microscopy (SEM), including energy dispersive X-ray analysis (EDX) and VIS-NIR spectroscopy.

An opal with a sphere diameter of 380 nm filled with amorphous  $\text{Sb}_2\text{S}_3$  is shown in Figures 1a and 1b. The as-prepared material is amorphous and granular in appearance. Further improvement in the optical properties of the composites was attained upon crystallization by annealing the amorphous synthesized material. This process provides an increase in the dielectric constant of  $\text{Sb}_2\text{S}_3$ . As the final step, to obtain an inverse opal and achieve a higher  $\nu$ , the sample was dipped in a hydrofluoric acid solution (1 wt.-%) for 7 h. By means of this

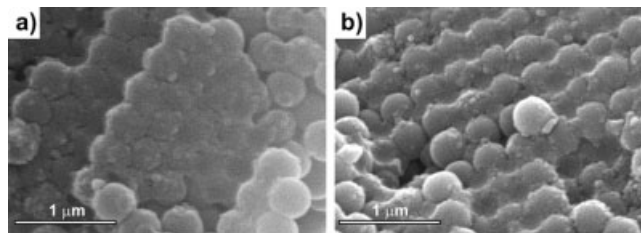


Fig. 1. SEM images of inner {111} (a) and {100} (b) planes of an opal matrix infilled with amorphous  $\text{Sb}_2\text{S}_3$ .

procedure, the silica spheres were removed, resulting in a new structure made of interconnected air spheres. SEM images of (111) and (100) surfaces of an inverted structure are shown in Figure 2. The crystalline form shows a smoother appearance (Fig. 2) than the granulated amorphous material (Fig. 1).

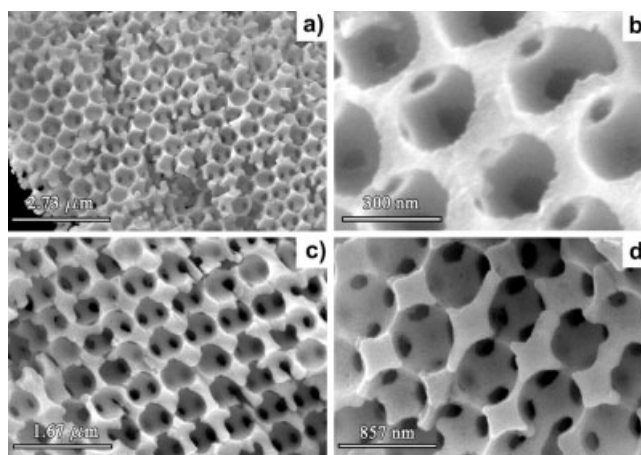


Fig. 2. SEM images of different orientations of a stibnite inverse opal: a,b) {111} facets; c,d) {100} facets.

To ascertain the quality of the amorphous and crystalline  $\text{Sb}_2\text{S}_3$ , characterization of the material was performed using Raman spectroscopy with the 514.5 nm line of an  $\text{Ar}^+$  laser. In Figure 3 the spectra of amorphous and crystalline stibnite synthesized here are shown and compared with commercial standard. Figure 3a shows the Raman spectrum of amorphous  $\text{Sb}_2\text{S}_3$  in a silica–amorphous  $\text{Sb}_2\text{S}_3$  composite and Figure 3b that of the crystallized and inverted material. The former presents a broad peak characteristic of amorphous material. The Raman spectrum of commercial stibnite is also plotted (Fig. 3c) and is identical to that synthesized in this work (Fig. 3b).

The elemental composition of the inverted opals was studied by EDX. The absence of a  $\text{Si K}\alpha$  peak in the EDX spectrum reveals that chemical etching of the composite is complete and all silica has been removed in the inverted opal. Additionally, the only peaks detected in the EDX spectrum, shown in Figure 4, are assigned to S and Sb. In Figure 4, the EDX spectrum of a sample of  $\text{Sb}_2\text{S}_3$  standard has also been included for comparison. A single peak at 2.3 keV is evidenced and is assigned to  $\text{SK}\alpha$  while a group of four peaks located in the region of higher energy is assigned to  $\text{SbL}\alpha$ .

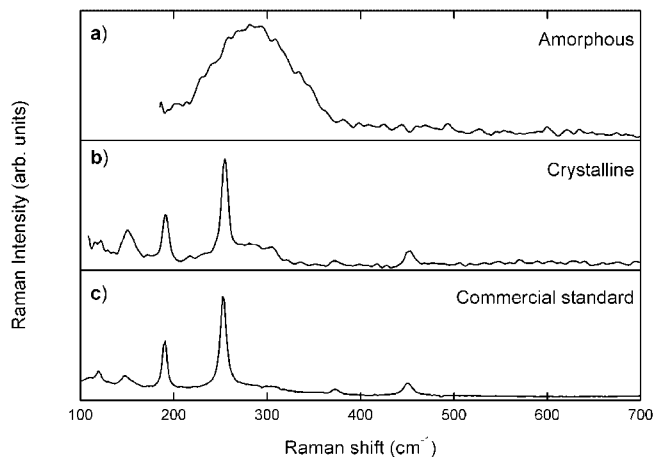


Fig. 3. Raman spectra of amorphous (a) and crystalline (b)  $\text{Sb}_2\text{S}_3$  compared with the commercial product (c).

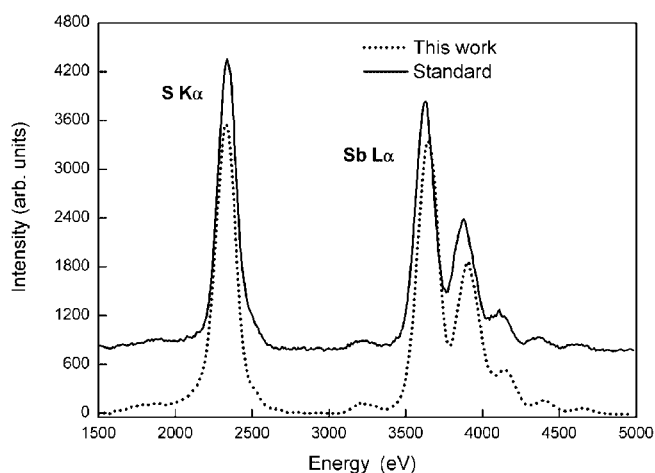


Fig. 4. EDX spectrum of synthesized crystalline  $\text{Sb}_2\text{S}_3$  inverted opal compared with standard commercial product. Spectra are vertically shifted for the sake of clarity.

These EDX spectra were recorded from large sample areas, consequently representing an average elemental composition of the antimony sulfide. The relative intensity of S and Sb peaks in the studied and reference samples is identical, suggesting that a stoichiometric sulfide is present in the inverted opal. Additionally, different point analysis and line profiles of the  $\text{S K}\alpha$  and  $\text{Sb L}\alpha$ , not shown, revealed no significant changes in composition, indicating that the studied sample is homogeneous.

Additional characterization of the material was performed by X-ray powder diffraction to verify the quality of the  $\text{Sb}_2\text{S}_3$  grown. The usual size of the opal bits used for infiltration is  $5\text{--}9\text{ mm}^2$  in surface area by  $0.5\text{ mm}$  thickness. This is clearly not enough for X-ray characterization. Even more so if we consider that at most only 26% of it will be  $\text{Sb}_2\text{S}_3$ . So, we synthesized  $\text{Sb}_2\text{S}_3$  out of the opal following exactly the same recipe and conditions for the annealing treatment. A broad peak in the diffraction pattern indicates the amorphous nature of the as-grown material. Upon crystallization of the material,

the diffraction pattern showed narrow and well-defined peaks, in good accord with those of the standard.

Optical reflectance measurements were carried out not only for the mere purpose of characterization at various stages of fabrication but to analyze the photonic properties of the opal-based structures. All the peaks described here correspond to features in the band structure. For a given lattice constant (determined by the spheres' diameter) the positions of the peaks are mainly determined by the average dielectric constant,  $\epsilon_{\text{av}}$ , and their widths are related to  $\nu$ .<sup>[29]</sup> Antimony trisulfide infiltrated opals present a broad and well-defined reflectance peak at low energies corresponding to first-order Bragg diffraction. This peak is much broader than that of the host bare opal and red shifted with respect to it. The magnitude of this shift (marked by the arrow in Fig. 5) permits the amount of infiltration attained to be assessed by knowing the dielectric functions of silica<sup>[30]</sup> and stibnite and the initial silica filling fraction, which is precisely controlled by the previous sintering of the host opal.<sup>[31]</sup>

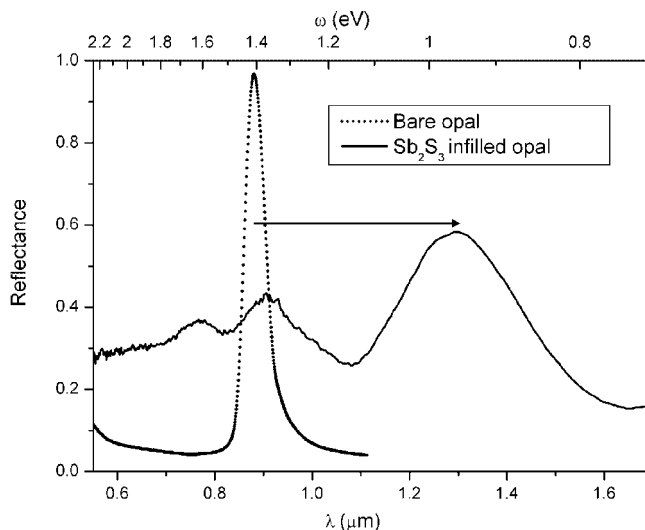


Fig. 5. Reflectance spectra from a  $410\text{ nm}$  diameter sphere bare opal (dotted line) and from the same opal loaded to ca. 80% of the pore volume with crystalline  $\text{Sb}_2\text{S}_3$  (continuous line). The arrow highlights the red-shift of the first stop band due to an increase of the average dielectric function after infiltration.

The reflectance measurements shown in Figure 5 present an example for a  $410\text{ nm}$  diameter silica sphere opal. The size of the beads was selected to avoid placing the relevant photonic bands features in the electronic gap of the material. As can be seen in the spectra, the bare opal shows a Bragg peak centered at  $0.88\text{ }\mu\text{m}$ . After opal infiltration and annealing, the peak of the crystalline composite is shifted to higher wavelengths. The width is also larger due to the increase in  $\nu$ .

In order to understand the photonic bandgap properties of the materials, full bandgap structure calculations<sup>[32]</sup> were performed for the different systems to be compared with the experimental results. In Figures 6 and 7, reflectance spectra are plotted next to the band structure of the corresponding system to allow direct comparison. Only the first 20 bands are plotted. In particular for the  $\text{SiO}_2\text{--Sb}_2\text{S}_3$  composite (Fig. 6)

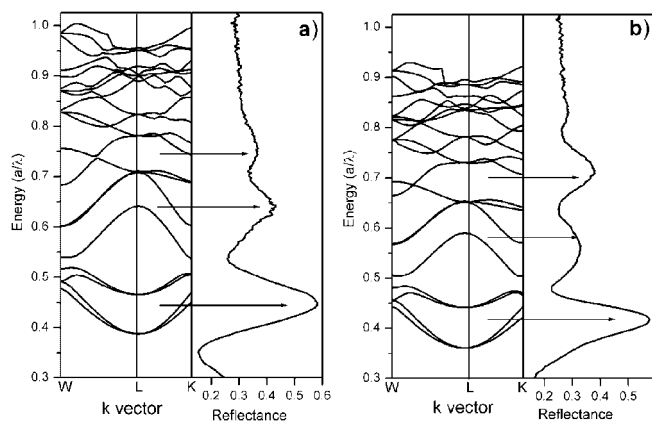


Fig. 6. Reflectance spectra from crystalline  $\text{Sb}_2\text{S}_3$ -silica opal made of 410 nm diameter spheres along with the band structures for 80 % (a) and 100 % (b) infiltrated opal. The marked regions highlight the correspondence between gaps in the band structure and the peaks in the spectra.

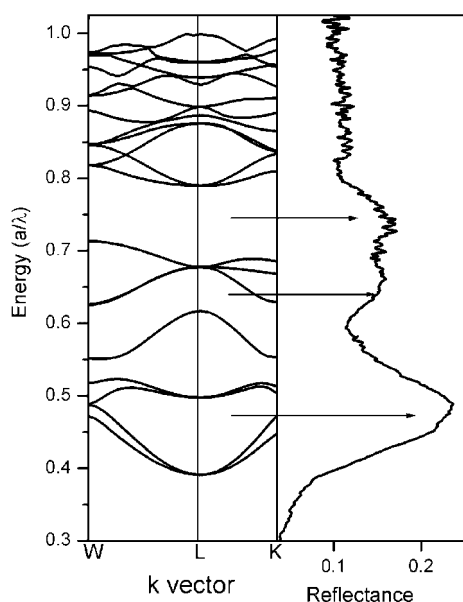


Fig. 7. Reflectance spectrum from crystalline  $\text{Sb}_2\text{S}_3$  inverted opal made of 410 nm diameter spheres and the band structure for a 100 % infiltrated region.

two representative spectra are plotted along with calculations assuming infiltration degrees of 80 % and 100 % in a sample of 410 nm diameter spheres. Although the material synthesized is very uniform in composition, infiltration is less uniform and can vary from point to point in the sample by a few percent. Owing to the high dielectric function of the guest material small variations in infiltration can lead to strong energy variations of the different band structure features. Although the two spectra shown here are qualitatively similar, a good assignment of the peaks can only be done on the assumption of such composition variations. The three peaks found are very plausibly assigned to the three gaps that open in or around the L point in the Brillouin zone. The magnitude and position of these gaps vary differently on departing from L toward different neighboring points, among which the most representative of the L symmetry are W and K, that being the

reason for the path chosen. The geometry of the experimental set up determines the range of wave vectors probed to be around half way between L and K or L and W. For that reason the arrows included in the diagrams are located approximately in the middle of the relevant gaps. The close correspondence between gaps and peaks supports the assignment.

For heavily infiltrated opals a process of inversion can be carried out by dissolution of the  $\text{SiO}_2$  in hydrofluoric acid. The resulting structure has a much higher dielectric contrast and, as a consequence, bands flatten out and gaps widen. This is shown in Figure 7. In particular, the second and third reflectance peaks from the composite all but merge in a single broad feature. This feature has a small dip in the center that can be accounted for by what can be seen as a bunch of bands isolated in the middle of a broad gap. The high energy part of this feature corresponds to the full gap that this structure presents. A display of the whole band structure shows that, in effect, this gap spans the whole Brillouin zone so that the peak observed would be present regardless of the direction in which reflectance was probed.

In conclusion, artificial opals were infiltrated with antimony trisulfide. This is one of the highest dielectric function materials with an electronic gap in the visible. A chemical bath deposition method for the growth of the stibnite was adapted. The material grown was characterized by standard means, revealing its crystalline structure and properties. The photonic bandgap properties of the composite and inverted structures agree with calculations. This material could be the first to allow the fabrication of photonic bandgap structures with a full gap in the visible.

### Experimental

The opals showed in this work were prepared following a method described previously [33,6].  $\text{Sb}_2\text{S}_3$  was grown by a method of precipitation in aqueous solution in which the opal was placed on a Pyrex porous plate (porosity around 100–120  $\mu\text{m}$ ) integrated in a funnel under vacuum.

The opal was first placed on the porous plate and soaked in 0.5 mL  $\text{SbCl}_3$  (35 wt.-%) solution ( $\approx \text{pH}$  1) at room temperature while suction was applied. Then, after drying the opal surface (in air) the same was done with the thioacetamide solution (2.0 M) at 55 °C ( $\approx \text{pH}$  5). Finally, the opal was heated at 65 °C for 20 min. After that the opal looked orange due to the amorphous nature of the inorganic  $\text{Sb}_2\text{S}_3$ .

It is worth mentioning that other reagents, concentrations, and solvents were explored. For the antimony source,  $\text{SbCl}_3$  was used not only in an aqueous medium, but also dissolved in acetone, ethylene glycol, acetic acid, and dilute sulfuric acid to yield antimony trisulfide with different solvent effects on the dissociation of  $\text{SbCl}_3$ . Sources of antimonyl ions as antimony(III) acetate were also tested. For sulfide ions sodium thiosulfate and thiourea were among the alternatives to the thioacetamide solution.

The annealing treatment was carried out in nitrogen atmosphere at 325 °C for 2 h in a tubular furnace.

The reference sample consist of a commercial  $\text{Sb}_2\text{S}_3$  (Aldrich 99 %+).

Optical spectroscopy, employed for the photonic band structure characterization, was carried out with the use of a Fourier transform spectrometer (Bruker IFS 66) to which a microscope was attached. The focalization and collection of reflected light was performed with a 36 $\times$  Cassegrain microscope objective. With this set up, incidence and reflectance is collected for all angles between 20° and 57°, which implies internal angles between 5° and 12°.

Received: June 4, 2002  
Final version: July 25, 2002

- [1] E. Yablonovitch, *Phys. Rev. Lett.* **1987**, *58*, 2059.
- [2] S. John, *Phys. Rev. Lett.* **1987**, *58*, 2486.
- [3] J. D. Joannopoulos, P. R. Villeneuve, S. Fan, *Nature* **1997**, *386*, 143.
- [4] J. G. Fleming, S. Y. Lin, *Opt. Lett.* **1999**, *24*, 49.
- [5] N. Yamamoto, S. Noda, A. Chutinan, *Jpn. J. Appl. Phys., Part 2* **1998**, *37*, L1502.
- [6] R. Mayoral, J. Requena, J. S. Moya, C. López, A. Cintas, H. Míguez, F. Meseguer, L. Vázquez, M. Holgado, A. Blanco, *Adv. Mater.* **1997**, *9*, 257.
- [7] a) F. García-Santamaría, C. López, F. Meseguer, F. López-Tejiera, J. Sánchez-Dehesa, H. T. Miyazaki, *Appl. Phys. Lett.* **2001**, *79*, 2309. b) F. García-Santamaría, H. T. Miyazaki, A. Urquía, M. Ibisate, M. Belmonte, N. Shinya, F. Meseguer, C. López, *Adv. Mater.* **2002**, *14*, 1144.
- [8] H. S. Sözüer, J. W. Haus, R. Inguva, *Phys. Rev. B* **1992**, *45*, 13962.
- [9] K. Busch, A. John, *Phys. Rev. B* **1998**, *58*, 3896.
- [10] O. D. Velev, T. A. Jede, R. F. Lobo, A. M. Lenhoff, *Nature* **1997**, *389*, 448.
- [11] J. Wijnhoven, W. L. Vos, *Science* **1998**, *281*, 802.
- [12] A. A. Zakhidov, R. H. Baughman, Z. Iqbal, C. Cui, I. Khairulin, S. O. Dantas, J. Marti, V. G. Ralchenko, *Science* **1998**, *282*, 897.
- [13] A. Blanco, E. Chomski, S. Grachtchak, M. Ibisate, S. John, S. W. Leonard, C. López, F. Meseguer, H. Míguez, J. P. Mondia, G. A. Ozin, O. Toader, H. M. van Driel, *Nature* **2000**, *405*, 405.
- [14] H. Míguez, E. Chomski, F. García-Santamaría, M. Ibisate, S. John, C. López, F. Meseguer, J. P. Mondia, G. A. Ozin, O. Toader, H. M. van Driel, *Adv. Mater.* **2001**, *13*, 1634.
- [15] O. Savadogo, K. C. Mandal, *J. Electrochem. Soc.* **1992**, *139*, L16.
- [16] M. T. S. Nair, Y. Peña, J. Campos, V. M. García, P. K. Nair, *J. Electrochem. Soc.* **1998**, *145*, 2113.
- [17] G. Ghosh, B. P. Varma, *Thin Solid Films* **1979**, *60*, 61.
- [18] R. S. Mane, B. R. Sankapal, C. D. Lokhande, *Thin Solid Films* **1999**, *353*, 29.
- [19] O. Savadogo, K. C. Mandal, *Sol. Energy Mater. Sol. Cells* **1992**, *26*, 117.
- [20] M. T. S. Nair, Y. Peña, J. Campos, V. M. García, P. K. Nair, *J. Electrochem. Soc.* **1998**, *145*, 2113.
- [21] J. D. Desai, D. D. Lokhande, *Thin Solid Films* **1994**, *237*, 29.
- [22] P. Arun, A. G. Vedeshwar, *J. Non-Cryst. Solids* **1997**, *220*, 63.
- [23] I. K. El Zawawi, A. Abdel-Moez, F. S. Terra, M. Mounir, *Thin Solid Films* **1998**, *324*, 300.
- [24] C. H. Bhosale, M. D. Uplane, P. S. Patil, C. D. Lokhande, *Thin Solid Films* **1994**, *248*, 137.
- [25] V. V. Killedar, C. D. Lokhande, C. H. Bhosale, *Mater. Chem. Phys.* **1997**, *47*, 104.
- [26] S. Mahanty, J. M. Merino, M. León, *J. Vac. Sci. Technol. A* **1997**, *15*, 3060.
- [27] K. Y. Rajpure, A. L. Dhebe, C. D. Lokhande, C. H. Bhosale, *Mater. Chem. Phys.* **1998**, *56*, 177.
- [28] G. H. Aylward, T. J. V. Findlay, in *SI Chemical Data*, John Wiley and Sons Australia, Ltd., Milton **1971**, p. 105.
- [29] J. D. Joannopoulos, R. D. Meade, J. N. Winn, in *Photonic Crystals: Molding the Flow of Light*, Princeton University Press, Princeton, NJ **1995**.
- [30] F. García-Santamaría, H. Míguez, M. Ibisate, F. Meseguer, C. López, *Langmuir* **2002**, *18*, 1942.
- [31] H. Míguez, F. Meseguer, C. López, A. Blanco, J. S. Moya, J. Requena, A. Mifsud, V. Fornés, *Adv. Mater.* **1998**, *10*, 486.
- [32] S. G. Johnson, J. D. Joannopoulos, *Opt. Express* **2001**, *8*, 173.
- [33] W. Stöber, A. Fink, E. Bohn, *J. Colloid Interface Sci.* **1968**, *26*, 62.

## Fast Proton Conductors Derived from Calcium Phosphate Hydrogels

By Toshihiro Kasuga,\* Masashi Nakano, and Masayuki Nogami

Much attention has been paid to polymer electrolyte fuel cells (PEFCs) using a series of perfluorinated ionomers such as Nafion<sup>®</sup> as possible separators. There are still problems

with electrolyte materials in terms of practical use because of chemical and mechanical degradation during prolonged usage. Fast proton conducting glasses are great potential candidates for the electrolyte because they easily form films and plates. Proton conduction in some amorphous materials such as zirconium phosphate or silica-based gel glasses<sup>[2,3]</sup> has been reported. In 1996,<sup>[4]</sup> zirconium phosphate gel glasses with high conductivities of  $\sim 10^{-2}$  S cm<sup>-1</sup> at room temperature were prepared for the first time using a sol-gel method, and it was emphasized that the conductivities were achieved by fast proton mobility in the phosphates containing hydrogen-bonded protons and a large amount of water. Since then, the role of P<sub>2</sub>O<sub>5</sub> in proton conduction in sol-gel derived glasses has been discussed and verified.<sup>[5]</sup> It was suggested that protons dissociated from SiOH and/or POH bonds in the glasses form ionic radicals such as H<sub>3</sub>O<sup>+</sup> in water and are transferred by hopping through water molecules.<sup>[5]</sup> The proton dissociation energy is determined by the hydrogen-bonding strength of the hydroxyl bonds. Phosphorus ions are one of the candidates as strong hydrogen bonding ions and they should increase the proton conductivity.<sup>[4,5]</sup> The performance of the H<sub>2</sub>/O<sub>2</sub> fuel cell using mesoporous phosphosilicate glasses showing high conductivities of  $\sim 2 \times 10^{-2}$  S cm<sup>-1</sup> at 30 °C at 70 % relative humidity (RH) was reported recently.<sup>[6]</sup> Some silica-based gel composites with high conductivities containing organic polymers have also been reported.<sup>[7-9]</sup> Although these glass-based materials have advantages in terms of high chemical durability and easy shaping ability, it may be necessary for practical use to improve their mechanical brittleness.

As described above, fast proton conductors can be developed by preparation of chemically stable inorganic materials containing large amounts of POH groups and water molecules.<sup>[4,6]</sup> Although heteropolyacid hydrates such as H<sub>3</sub>Mo<sub>12</sub>-PO<sub>40</sub>·29 H<sub>2</sub>O, H<sub>3</sub>W<sub>12</sub>PO<sub>40</sub>·29 H<sub>2</sub>O,<sup>[10]</sup> and H<sub>2</sub>UO<sub>2</sub>PO<sub>4</sub>·4H<sub>2</sub>O<sup>[11]</sup> are typical examples of fast proton conductors ( $\sim 10^{-1}$  S cm<sup>-1</sup> even at room temperature), these materials are unstable in humidity and decompose at  $\sim 50$  °C. We anticipated that calcium phosphate hydrates such as Ca(H<sub>2</sub>PO<sub>4</sub>)<sub>2</sub>·H<sub>2</sub>O or Ca<sub>3</sub>(HP<sub>2</sub>O<sub>7</sub>)<sub>2</sub>·4H<sub>2</sub>O, which are more stable than the above-mentioned hydrates, may be noteworthy as new proton-conducting crystals, although their proton conduction has not been reported so far. In addition, if these hydrate crystals could be formed in glasses or gels having easy shapability into films and plates, the materials containing the crystals would have large potential for use as the electrolyte. In the present work, calcium phosphate hydrate crystals were found to be precipitated in CaO-P<sub>2</sub>O<sub>5</sub>-H<sub>2</sub>O gels,<sup>[12]</sup> which were derived from hydration of powders of the melt-quenched calcium metaphosphate glass, by heat treatment in wet atmosphere, and the crystallized products showed fast proton conduction and mechanical ductility.

Figure 1 shows an X-ray diffraction (XRD) pattern and a scanning electron microscopy (SEM) image after heat treatment of the glass-derived hydrogel at 90 °C for 6 h in saturated vapor. The SEM specimen was prepared using a freeze-drying method. The XRD pattern shows that the crystalline

\*] Prof. T. Kasuga, M. Nakano, Prof. M. Nogami  
Department of Materials Science and Engineering  
Nagoya Institute of Technology  
Gokiso-cho, Showa-ku, Nagoya 466-8555 (Japan)  
E-mail: kasugato@mse.nitech.ac.jp